Article

Holocene Glaucony from the Guadiana Shelf, Northern Gulf of Cadiz (SW Iberia): New Genetic Insights in a Sequence Stratigraphy Context

Adrián López-Quirós [1,2,*] , Francisco José Lobo [3] , Isabel Mendes [4] and Fernando Nieto [5]

1 Department of Geoscience, Aarhus University, Høegh-Guldbergs Gade 2, 8000 Aarhus, Denmark
2 Department of Stratigraphy and Paleontology, University of Granada, 18071 Granada, Spain
3 Instituto Andaluz de Ciencias de la Tierra, CSIC-UGR, 18100 Granada, Spain
4 Centro de Investigação Marinha e Ambiental (CIMA), Universidade do Algarve, 8005-139 Faro, Portugal
5 Department of Mineralogy and Petrology, University of Granada, 18071 Granada, Spain
* Correspondence: alquiros@geo.au.dk or alquiros@ugr.es

Abstract: Glaucony occurrences have been reported both from exposed transgressive and overlying highstand system tracts. However, its occurrences within highstand deposits are often invoked as the result of underlying condensed section reworking. Detailed textural, mineralogical and geochemical reports of glaucony grains in highstand deposits remain elusive. The northern Gulf of Cadiz shelf (SW Iberia) offers a unique opportunity to investigate late Holocene glaucony authigenesis in a well-documented time-stratigraphic context, where transgressive deposits are locally exposed on the seafloor and are laterally draped by highstand muddy deposits. In this study, glaucony grains extracted from a core retrieved from a highstand muddy depocenter off the Guadiana River were investigated by means of digital microscopy, X-ray diffraction (XRD), and electron microscopic methods (FESEM-EDX and TEM-HRTEM). To better constrain the glaucony origin (autochthonous vs. allochthonous) in highstand muddy deposits, glaucony grains from surficial samples—taken from exposed transgressive deposits—were also investigated. Glauconitization in the studied core can be largely attributed to the replacement of faecal pellets from c. ~4.2–1.0 cal. ka BP. Both XRD and TEM-HRTEM analyses indicate that glaucony consists mainly of an R1, with a minor presence of R0, smectite-rich (nontronite) glauconite-smectite mixed-layer silicate, made up of 35–75% glauconitic layers and 65–25% of interstratified smectite layers. At the mineral lattice level, minor individual 7Å layers (berthierine) were also identified by HRTEM. Shallow radial cracks at the pellet surface, along with globular and vermiform-like biomorphic to low packing density lamellar-flaky nanostructures, mineralogical properties, and K-poor content (average 0.4 atoms p.f.u.) indicate a scarcely mature glauconitization process, attesting to formation of the grains in situ (autochthonous). Glaucony grains from exposed transgressive deposits, i.e., in the tests of calcareous benthic foraminifera, do not share a genetic relationship with the grains investigated in the highstand deposits, thus supporting the autochthonous origin of glaucony within the highstand deposits. Our combined dataset provides evidence of a multiphase history for autochthonous glaucony formation in the Guadiana shelf, as its genesis is traced to both transgressive and highstand conditions. While eustatic sea-level changes favoured glaucony formation under transgressive conditions, factors such as protracted low sediment supply and the establishment of a strong nutrient-rich upwelling system in the study area promoted glaucony development during late Holocene highstand conditions.

Keywords: glaucony; sequence-stratigraphy; HST; continental shelf; Gulf of Cadiz; Holocene

1. Introduction

With the increasing application of sequence-stratigraphic concepts to sedimentary successions, authigenic clay minerals, including glaucony-bearing facies, have become

reliable indicators of significant strata-bounding surfaces such as maximum flooding surfaces or condensed sections [1–8].

Major requirements for glaucony development include: (1) low accumulation rates of detrital sediments; (2) prolonged residence times ($<10^4$ years for a mature stage; [9]) of detrital grains close to the sediment-sea water interface; (3) existence of a granular substratum (carbonatic or siliciclastic; including the muddy infilling of carbonate bioclasts) with high porosity and permeability; (4) redox potential (Eh) ~0 mV, (5) seawater pH 7–8; and (6) organic-rich, semiconfined microenvironments. These conditions are typically found in low-latitude, shallow-marine settings at water depths of 100–300 m, at temperatures lower than 15 °C, and under sub-oxic, partially reducing environments [8,10]. However, glaucony formation has also been reported in deep-sea environments at water depths of 2000–3000 m and temperatures lower than 6 °C [11–13], as well as in very shallow marine, estuarine [14–16] and paleosol [16] environments.

Recent studies have determined that although glaucony may be found in any part of a single depositional sequence as reworked deposits (allochthonous), glaucony grains with an in situ autochthonous origin are mainly associated with the Transgressive Systems Tract (TST) [1,7,10,11,17–21]. Transgressive conditions can favour widespread glaucony formation because of: (1) low sedimentation rates during relative sea-level rises due to significant drops in detrital input [7,10,11,22,23], preventing rapid sediment burial that would halt the glauconitization process; (2) progressive availability of shallower substrates at the sediment-water interface; and (3) recurrent bottom current winnowing [11,22,23]. Autochthonous glaucony is rarely documented in omission surfaces at the base of parasequences in lower Highstand Systems Tracts (HSTs) or in upper HSTs [1,7].

On the continental shelf off the Guadiana River (northern Gulf of Cadiz, SW Iberia), Holocene sea-level changes combined with local factors led to the formation of both postglacial TST and HST [24–26]. Within the TST, several transgressive deposits are exposed across the inner to middle shelf [24,27,28]. Highstand deposits occur on the inner shelf as a prodeltaic wedge and on the middle shelf as elongated muddy belts [25,27,29,30]. Glaucony formation in the Guadiana shelf was initially described in the post-glacial TST [27]. More recent studies report that glauconitization also took place during HST formation in the Guadiana Shelf [29]. In view of previous evidence, we aim to provide a more consistent characterization of glaucony occurrences in the Guadiana Shelf by integrating nano-structural, mineralogical, and geochemical datasets.

The objectives of our multi-proxy approach are (1) to determine the effect exerted by the parent substrate material on the chemical variability and maturity of glauconitic grains; and (2) to seek the factors controlling the source, (bio)availability, and geochemical behaviour of iron and other chemical elements required for the glauconitization process during advanced highstand conditions on continental shelves, which are thought to be largely unfavourable for glaucony authigenesis. In order to rule out the allochthonous origin of the glaucony occurrence at the HST (due to penecontemporaneous remobilizations of glaucony grains from the TST), glaucony grains from surface samples retrieved from exposed transgressive deposits on the Guadiana shelf are also investigated.

2. Geological Setting and Stratigraphic Framework

2.1. Shelf Sediment Sources

The study area lies in the middle shelf on the northern margin of the Gulf of Cadiz, close to the Guadiana River mouth, southwestern Iberian Peninsula (Figure 1). The Guadiana River is a major regional sediment source for the continental shelf, draining a semi-arid region influenced by both small-scale seasonal climatic variations and large-scale ones such as the North Atlantic Oscillation [31,32]. Sediment bypasses the channel of the Guadiana River estuary during episodic floods, thus playing a key role in sediment supply from the river to the adjacent shelf [33,34]. Littoral drift provides further sediment to the shelf, mainly of sands that are transported eastward along the Portuguese coastline [35].

2.2. Surficial Sediment Distribution and Glaucony Occurrences

Contemporary sediment distribution patterns are influenced by physiographic changes and river discharges [27]. Sediments of the inner shelf off the Guadiana River mouth at water depths < 10 m are mainly terrigenous quartzose fine sands. At 10–30 m water depths, several coarse-sand patches are found, where quartz remains the most abundant component (Figure 1b). West and east of the river mouth, sandy sediments are substituted by fine sediments (silts and clays) with greater proportions of quartz (Figure 1b; [27]). The middle shelf (30–100 m water depth) is characterized by an extensive mud belt. To the east of the Guadiana River, it is cut from north to south by a strip of muddy and gravelly sands (Figure 1b) due to partial seafloor exposure of a transgressive bulge (Figure 1b–d; [27]). The proportion of sand-size grains in the mud belt is very low (Figure 1b) and is mainly composed of foraminiferal tests [27], while the outer shelf below 100 m water depth is mostly covered by silty sands (Figure 1b; [27,36]).

Glaucony grains are found in large quantities in the northern shelf of the Gulf of Cadiz (Figure 1c; [27]). The proportion of glaucony is highest on the outer shelf, with maxima to the south of the Guadiana Estuary mouth and to the south of the transgressive bulge, where the main glaucony depocenter is located—with as much as 16% of glaucony grains (Figure 1c). Glaucony occurrences decrease eastward along the outer shelf and landward across the transgressive bulge, from 10% to 5% (Figure 1c).

2.3. Oceanographic Conditions

Surface circulation along the northern shelf of the Gulf of Cadiz has a cyclonic pattern [37]. Inner shelf waters (<30 m water depth) are strongly influenced by short-time fluctuations of the wind regime. Under westerlies dominance, coastal upwelling in the Algarve and Guadiana shelves is recurrent [38,39]. In the Guadiana shelf, upwelling induces primary production through the vertical advection of nitrate-rich sub-thermocline waters (Figure 1a; [38,40]). Those upwelled waters favour the formation of coastal jets moving equatorward [41]. Under easterlies dominance, the inner shelf is periodically affected by poleward coastal counter-currents along the coast [42]. The outer shelf is swept by the Gulf of Cadiz Current (GCC), a branch of the Portuguese-Canary eastern boundary current that transports Eastern North Atlantic Central Waters towards the Strait of Gibraltar [43].

2.4. Postglacial Evolution: Sediment Deposition Controlled by Sea-Level and Climatic Changes and by Anthropogenic Activities

The postglacial evolution of the northern shelf of the Gulf of Cadiz comprises transgressive and highstand stages bounded at about 6.5 calibrated kilo-years before present (cal. ka BP) [44,45]. Off the Guadiana River, several shallow-water deposits showing a backstepping stacking pattern from the outer to middle shelf have been related to the postglacial transgression [24]. In the outer shelf, the oldest transgressive deposit predates a period of rapid sea-level rise during melt-water pulse (MWP)-1A [46]. Subsequently, two pre-Holocene fine-grained shallow water deltas formed during periods of reduced rates of sea-level rise in a time interval (13.8–11.2 cal. ka BP) before and after the Younger Dryas event [28]. These deltaic deposits likely evolved laterally to fine-grained depocenters [47].

The transition to the Holocene witnessed the deposition of two additional coarse-grained paleo-Guadiana deltaic deposits between 11.2 and 8.8 cal. ka BP, under conditions of rapid sea-level rise during MWP-1B [28]. In the Guadiana River Estuary, this interval of sea level rise was recorded by a clayey sediment infilling from 9.8 to 7.5 cal. ka BP, followed by the introduction of coarser sediments during 7.7–7 cal. ka BP [48]. The rapid sea-level rise terminated at about 6.5 cal. ka BP, with a conspicuous phase of coastal progradation recognized along the southern coasts of the Iberian Peninsula [44,49].
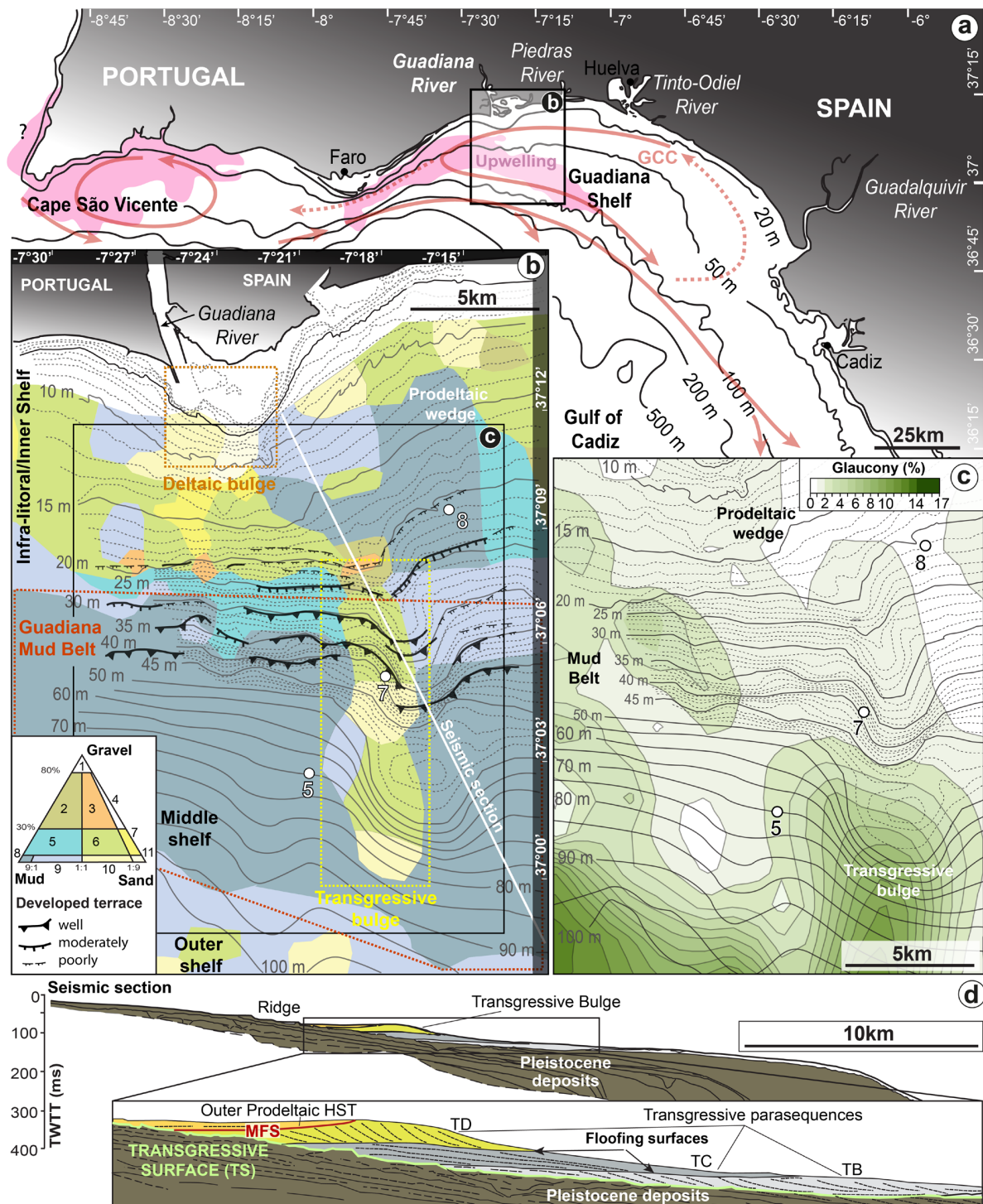
Figure 1. (**a**) Location map of the continental shelf off the Guadiana River, in the northern Gulf of Cadiz (SW Iberia). The pink area indicates schematic position of the present-day upwelling conditions [38]. Flow paths of the Gulf of Cadiz Current (GCC) are indicated by red arrows [41,43]. (**b**) Physiography of the Guadiana shelf along with distribution of surface sediments (adapted from Gonzalez et al. [27]). Legend: (1) gravel, (2) muddy gravel, (3) slightly muddy sandy gravel, (4) sandy gravel, (5) gravelly mud, (6) slightly muddy gravelly sand, (7) gravelly sand, (8) mud 'silt and clay', (9) sandy mud, (10) muddy sand, (11) sand. Location of the studied core, along with referred cores in the study area. (**c**) Distribution of glaucony-forming grains on the Guadiana shelf (from Gonzalez et al. [27]). (**d**) Seismic stratigraphic sub-surface architecture of the continental shelf off the Guadiana River (modified from Gonzalez et al. [27] after Lobo et al. [24]). MFS: Maximum flooding surface; TB, TC, and TD: backstepping transgressive deposits (parasequences, from older to younger).

The Holocene sea-level stabilization has been framed in the last 6.5 cal. ka BP. In this region, the Holocene highstand featured an initial phase of slow sea-level rise at 6.5–5 cal. ka BP, followed by a stillstand [48,50,51]. After 4.0 cal. ka BP, episodes of marked aridity, together with anthropogenic influences, led to environmental changes in the Guadiana River basin [52]. During the late pre-Roman, Roman, Moorish, and early Portuguese settlement stages (~3.0–0.3 cal. ka BP), deforestation/exploitation of timber plus extensive farming triggered widespread erosion and the concomitant silting up of estuaries in the Algarve region [53]. In the upper domain of the Guadiana Estuary, widespread erosion and soil loss may be the main reasons behind the abandonment of rural villages during the mid-12th century [54].

On the shelf, deposition during the Holocene highstand resulted in the major growth of diverse depositional systems. Off the Guadiana River, the main depositional bodies related to this phase are muddy belts developed on both sides of the transgressive bulge (Figure 1b; [25]) after the maximum flooding at around 6.5 cal. ka BP [30]. Diverse sedimentary records indicate temporally changing sedimentation rates, with low sedimentation rates for at least about 4 ka, and subsequent increases driven by climatic anomalies and by human activities such as mining and agriculture [30,47,55]. Specifically, dramatic increases in sediment supply are recognized after the Medieval Period [30,32,56]. Additional conspicuous evidence of Pb and Cu enrichments would be related to Roman and modern mining activities [57,58].

3. Material and Methods

In the study area, three cores were collected from the continental shelf off the Guadiana River in July 2002 (cores 5, 7 and 8; Figure 2), by using a light-weighted vibrocorer with water injection. These cores cover the different shelf depositional environments [29]. Core 5, 353 cm long, was taken from the middle shelf mud belt at a 72-m water depth (latitude 37°1′54″ N and longitude 7°20′44″ W) and comprises the last ca. 11.5 cal. ka BP (Figure 2a). Core 7, 71.5 cm long, was taken from the proximal zone of a transgressive sandy deposit [24,27] at a 36-m water depth (37°3′44″ N, 71°7′40″ W), and comprises the last ca. 10.4 cal. ka BP (Figure 2b). Core 8, 376 cm long, was extracted from the inner shelf prodeltaic wedge at a 22-m water depth (37°7′24″ N, 7°16′6″ W), and comprises the last ca. 5.0 cal. ka BP (Figure 2c). Further details on the age models can be obtained from Mendes et al. [29].

The present study focuses on sediments encompassing glaucony grains. Of the three cores, glaucony grains are found only in core 5 (Figure 2; [29]), mostly deposited under highstand conditions. The glaucony-bearing samples were selected from different stratigraphic positions (Figure 3a) in order to study potential textural and compositional differences. Glaucony grains were extracted from the sediment samples after sieving the 63–2000 μm fraction. Size fractions >63 μm were later separated magnetically, using an Isodynamic Laboratory Separator Model L-1 (S.G. Frantz®, Tullytown, PA, USA). Purified glaucony grains were further separated from diagenetic complex growths and aggregates along with other terrigenous grains under digital microscopy.

Isolated glaucony concentrates were studied in nine sediment samples under the digital microscope for morphological characterization. In addition, the textures of the isolated glaucony grains were examined under scanning- and transmission-electron microscopes. Several photomicrographs of the glauconitic sediments were taken with an Invenio 6EIII –6.3 MP camera (DeltaPix, Smorum, Denmark) connected to a 3D Digital Microscope (DeltaPix, Smorum, Denmark) and captured with *InSight* image-management software (DeltaPix, Smorum, Denmark). Secondary electron (SE) photomicrographs of isolated glaucony grains were obtained with a field emission scanning electron microscope (FESEM) GEMINI (ZEISS, Oberkochen, Germany). Transmission electron microscopy (TEM-HRTEM) photomicrographs were obtained using a TALOS F200X featuring a high-angle annular dark field (HAADF) detector, working at 200 kV, with a point-to-point resolution of 0.12 nm

in the TEM mode and 0.19 nm in the scanning transmission electron microscopy (STEM) mode (Thermo Fisher Scientific, Waltham, MA, USA).

X-ray-diffraction (XRD) data were obtained from oriented aggregates of powder glaucony grain concentrates (reduced in size with an agate mortar), air-dried and treated with ethylene glycol, deposited onto a 0 background Si sample holder. They were recorded using a PANalytical X'Pert Pro diffractometer (CuKα radiation, 45 kV, 40 mA) equipped with an X'Celerator solid-state linear detector (Malvern Panalytical Ltd., Malvern, United Kingdom). XRD diagrams were collected for 10 s in 0.008° 2θ steps. In the case of superposed glauconite and smectite mixed-layer peaks, phase identification and intensity measurements of each individual peak were carried out with the help of decomposition routines included in *HighScore* 5.1. software. Peaks were fitted through a Voigt function (mixed Gaussian (G) and Lorentzian (L)). Various combinations of peaks were proven before acquiring the lowest residuum. Intensity, G/L proportion, half-height width, and peak position were approximated by the least-squares method until they optimally retraced the peak course of the original profile.
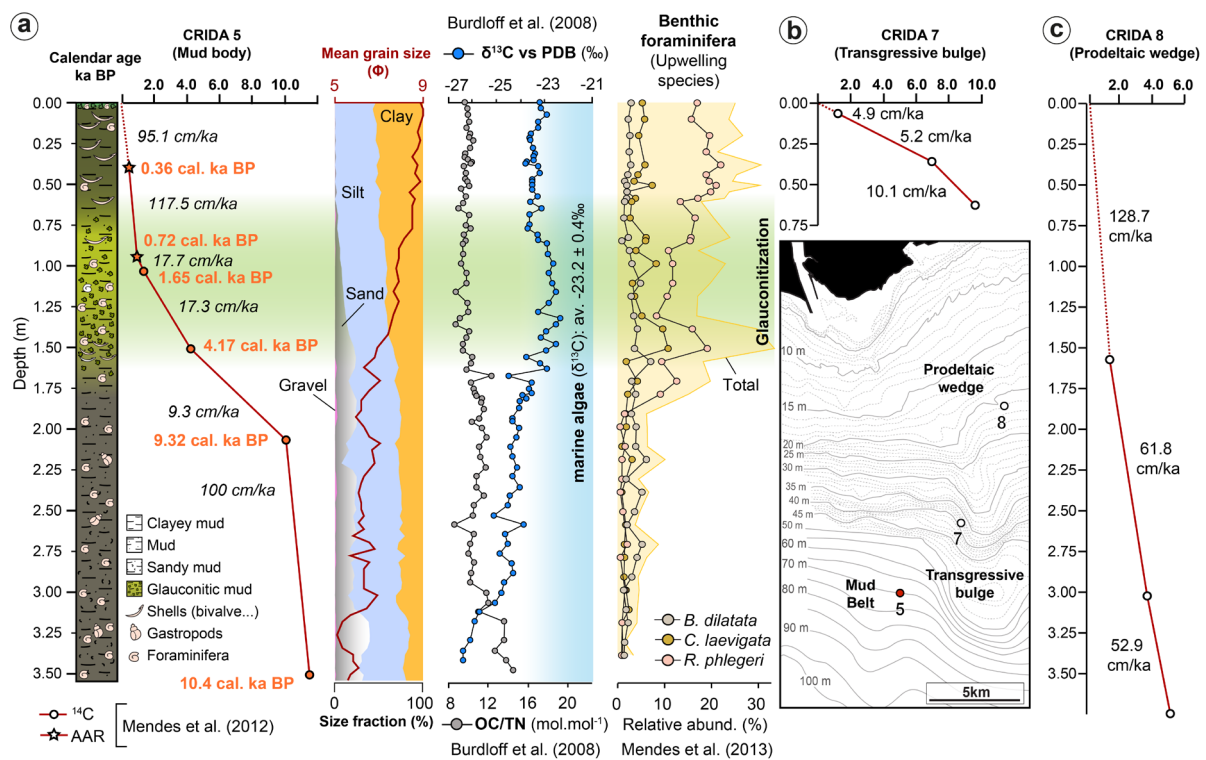

Figure 2. Contrasting sedimentary environments on the continental shelf off the Guadiana River. (**a**) Core 5 (middle shelf mud belt). (**b**) Core 7 (proximal zone of a transgressive sandy deposit). (**c**) Core 8 (inner shelf prodeltaic wedge). Age models based on calibrated ages and sedimentation rates are included (adapted from Mendes et al. [29]). In (**a**), bottom-up variation in size fractions and mean grain size [29], δ13C and OC/TN concentrations (<63 μm fraction of carbonate-free samples; [47]), and relative abundance (%) of benthic foraminiferal species associated with upwelling conditions [55] are also indicated. The glauconitization process is highlighted.

Qualitative elemental analyses of the main glaucony-forming elements were obtained through the above-mentioned FE-SEM GEMINI (ZEISS, Oberkochen, Germany), equipped with an energy-dispersive X-ray spectroscopy system (EDX). To complete the compositional study, the same powder used for the XRD analyses was also used for quantitative chemical micro- to nano-analyses with a TALOS instrument in STEM mode (Thermo Fisher Scientific, Waltham, USA). Powdered glaucony concentrates were first dispersed in an ethanol solution, then sonicated, and deposited on a thin carbon film coated upon several Cu grids. Quantitative micro- to nano-chemical analyses, in STEM mode, were acquired by

means of the AEM-EDX, using the Super-X detector. Mineral standards were used to obtain K-factors according to the method proposed by Lorimer and Cliff [59]. The crystal-chemical structural formula, based on AEM analysis, was calculated on the basis of a half-unit cell with 10 oxygen atoms and 2 hydroxyls (22 negative charges) per formula unit, and assuming total Fe to be Fe^{3+}.
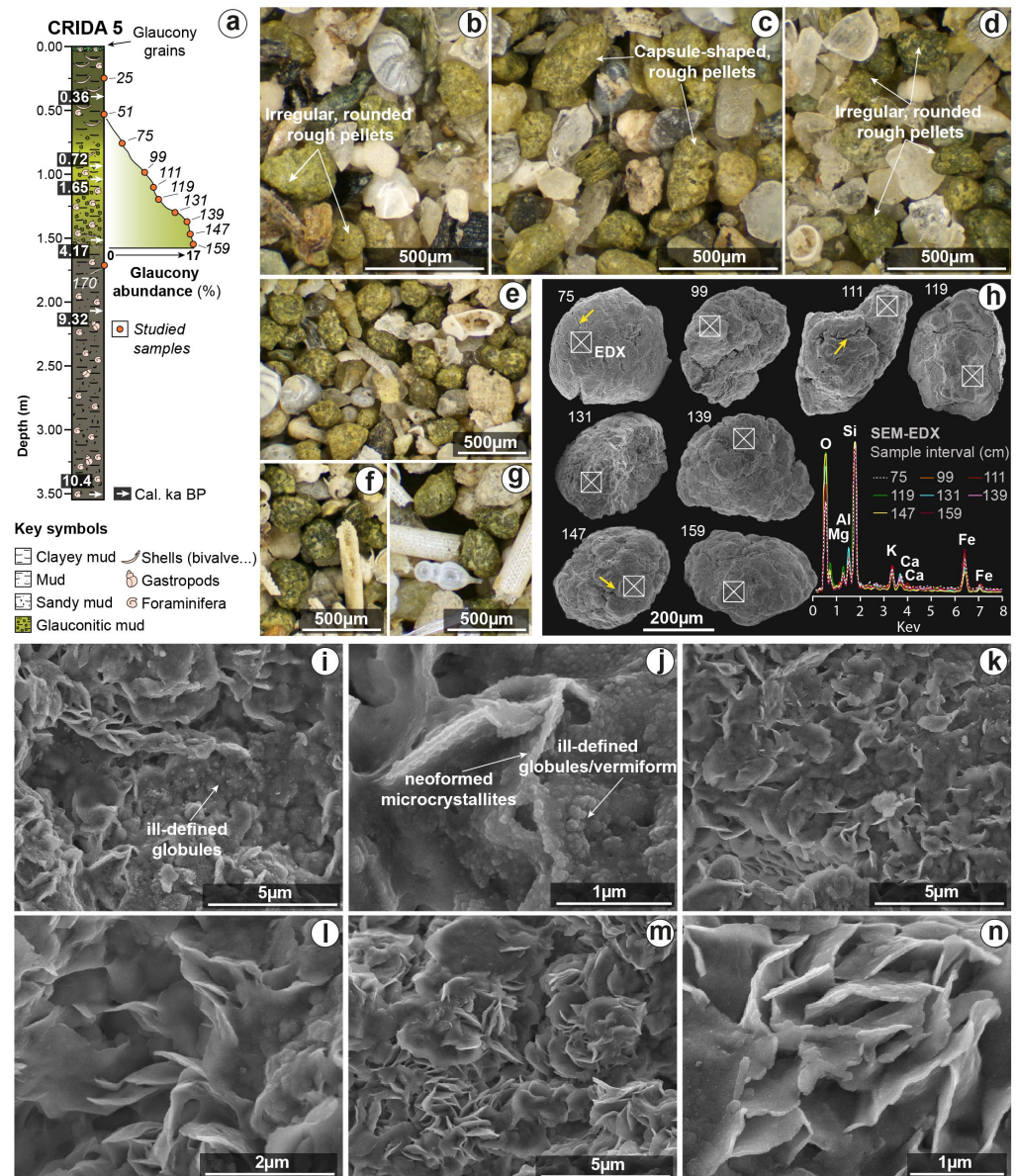

Figure 3. (**a**) Simplified lithological log of investigated core 5 (Guadiana mud belt). Glaucony abundance and sample location are highlighted. Age model is from Mendes et al. [29]. (**b**–**g**), Digital images showing the >63 µm size fraction of the investigated glaucony-bearing muddy sediments. Glaucony is mainly formed by irregular rounded to capsule-shaped, yellowish to light green grains. Note that other terrigenous components and microfossils such as foraminifera are present. (**h**) SEM photomicrographs (SE) of sieved and purified glaucony grains showing irregular rounded grains with rough surfaces. Poorly evolved radial cracks (yellow arrows). Corresponding energy dispersive X-ray (EDX) analysis of each grain is shown. (**i**–**n**), SEM photomicrographs (SE) displaying detailed surface nanostructures of glaucony grains. (**i**–**k**), Detailed view of ill-defined globules and vermiform nanostructures. Note the development of low packing size/density lamellar-flaky nanostructures from ill-defined globules/vermiform structure. (**l**–**n**), Detailed view of flakes (~1 µm long).

In order to assess potential penecontemporaneous remobilizations of glaucony grains from older to younger sediments (i.e., from transgressive to highstand deposits), seven surface sediment samples collected across the distal transgressive sandy deposit, covering a water depth range from 74 to 167 m, were investigated. The same laboratory procedure (XRD and FESEM-EDX) was adopted as for the core-derived samples.

4. Results and Interpretation

4.1. Core 5: Holocene Glaucony Occurrences

4.1.1. Glaucony Abundance, Grain Type, Morphology and Nanostructure

The relative abundance of glaucony grains within core 5 decreases upward from a 160-cm depth (<17%) to a 75-cm depth (<5%) (Figure 3a). Overall, glauconitized grains occurred as medium sand-sized grains ranging in diameter from ~200 to 400 μm (Figure 3b–h). Glaucony is mostly formed by irregular rounded to capsule-shaped, yellowish to light green grains with poorly evolved radial cracks (Figure 3b–h) having rough surfaces (Figure 3h) and a low packing density lamellar-flaky nanostructure with 1 μm long flakes (Figure 3i–n). Glauconitic clay fakes generally display a veil-like or film morphology with curled edges (Figure 4a) according to the nomenclature by Buatier et al. [60]. Moreover, distinctive lath-like glauconite particles were observed, taking advantage of their perpendicular orientation (Figure 4a). Corresponding EDX-maps were also obtained from the particles, showing representative variations in Al and Fe (Figure 4b). Lattice images of individual crystals exhibit well-defined ~10Å fringes, characteristic of both mica-type and contracted smectite layers (i.e., interstratified glauconite-smectite; Figure 4c–f). Interstratified (individual) 7Å-berthierine layers were recognized as well (Figure 4c–f). The preservation of ill-defined globular and vermiform biomorphic nanostructures was recorded (Figure 3i,j).

Glaucony in core 5 occurred through the preferential transformation of clay in faecal pellets (Figure 3b–h).

4.1.2. Glaucony Grain Mineralogy

Powder XRD air-dried diagrams of paramagnetic fraction rich in glaucony grains show a broad band that extends towards higher basal spacings, giving an average intensity maximum of 14.3Å (Figure 5a). The first-order basal reflection (d_{001} at 14.3Å) shifted to 16.3Å after ethylene-glycol treatment (Figure 5a). After deconvolution of the peaks of glaucony concentrates treated with ethylene glycol, the first basal reflection appears as an asymmetrical wide band with overlapping peaks (Figure 5b).

Deconvoluted peaks indicate that the glauconite contains expandable smectite layers. According to Moore and Reynolds [61], the XRD patterns may be interpreted as a distinctive poorly mature glauconite-smectite (mostly R1 ordered) mixed-layer phyllosilicate. The higher-order peaks of the mixed layers, which are diagnostic for the % of smectitic layers, comprise a wide band showing a continuum, rather than individual peaks, with a range of spacings roughly equivalent to 35–75% illite layers and 65–25% of interstratified smectite layers (Figure 5b). The extension of the first order peak up to the 16.3Å region is interpreted as indicating a minor component of R0-ordered glauconite-smectite. Overall, the wide range of interstratifications of glaucony corresponds to the different stages of maturation from nascent (most immature) to evolved (Figure 5b).

4.1.3. Glaucony Grain Chemical Composition and Structural Formulae

In core 5, glaucony pellets display mean concentrations of K_2O from ~3–4 wt %, while the Fe_2O_3 (total Fe) content gives a range of ~20–29 wt % (Table 1). The Fe_2O_3 content is thus moderate to high.
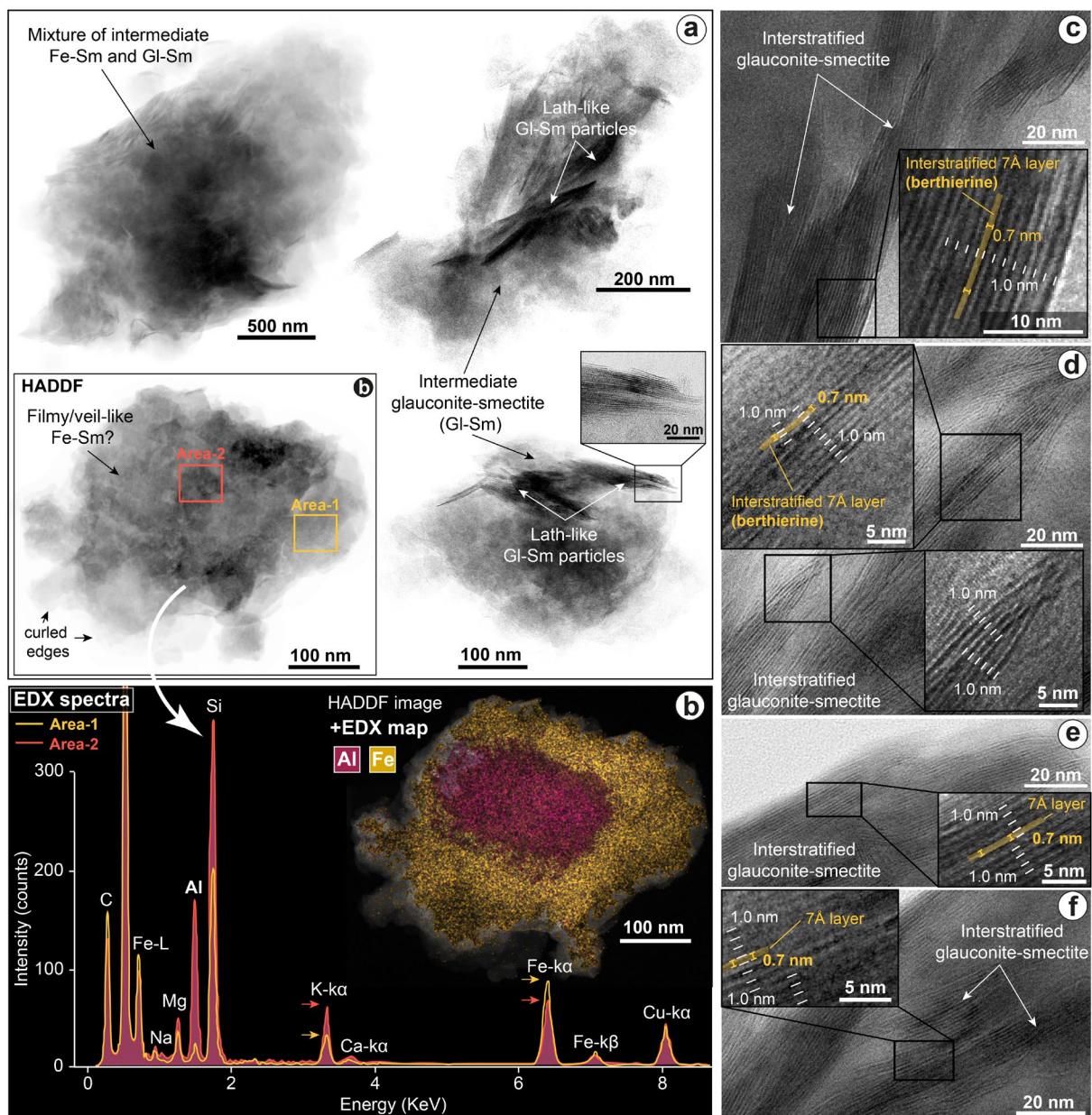
Figure 4. (**a**) TEM-HRTEM photomicrographs of representative individual clay particles from the glaucony-grain sub-fraction from core 5. These clay particles display a veil-like or film morphology with curled edges, as well as distinctive lath-like glauconite-smectite. (**b**) Representative energy dispersive X-ray (EDX) map (Al + Fe) of selected veil-like/filmy particles, showing variations in Al and Fe. (**c**–**f**), HRTEM lattice fringe images of individual crystals. Note that ~10Å fringes, characteristic of both mica and contracted smectite-layers, along with minor (individual) 7Å-layers of berthierine, are observed in the interstratified glauconite-smectite mixed layer.

The compositional relationship between K_2O versus total Fe expressed as Fe_2O_3 highlights the evolution of the glauconitization process [17]. The bivariate plot between K_2O and Fe_2O_3 exhibits a broad scatter, ranging from the field of immature (nascent sensu Odin and Matter [17]) smectite-rich glauconitic composition to a slightly evolved, glauconitic composition (Figure 6a), akin to the wide range of types and compositions obtained by XRD (Figure 5). The K_2O appears to be positively correlated with Fe_2O_3 (Figure 6a). In contrast, the Al_2O_3 content displays a significant negative correlation with Fe_2O_3 (Figure 6b). A negative correlation was likewise found between Al_2O_3 and K_2O, as well as with SiO_2 (Figure 6b).
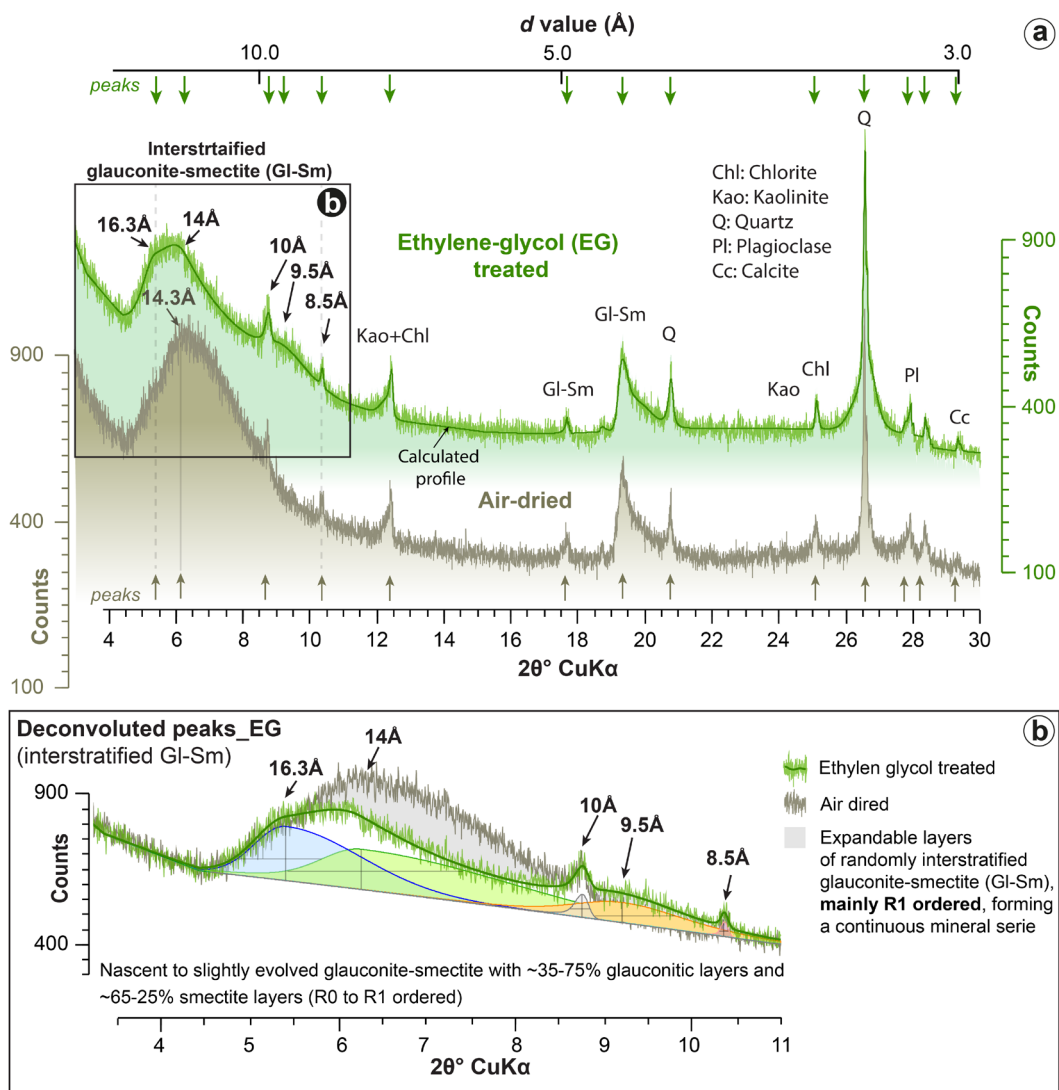
Figure 5. (**a**) Representative powder XRD diagrams of air-dried and ethylene-glycol treated glaucony concentrates from core 5, with notation of *d* value. Note the strong reflection at 14.3Å that shifted to 16.3Å after ethylene-glycol treatment, characteristic of smectite-rich interstratified glauconite-smectite. (**b**) Deconvoluted d_{001} peak and overlapping peaks after ethylene-glycol-treated glaucony. The strong response to ethylene-glycol treatment is indicative of expandable smectite layers. Deconvoluted peaks correspond mostly to R1, with minor presence of R0, mica/smectite.

Based on the AEM analysis, glaucony particles display a representative glauconite-smectite composition with copious substitutions of Fe^{3+} for Al in the tetrahedral site (Table 2). Chemical contamination by residual berthierine layers (Figure 4c–f)—whose correct normalization criteria is different to that of smectite and mica layers due to its trioctahedral nature—produces some anomalies in relation to the expected chemical composition of glauconite/smectite, in particular, depletion in ^{IV}Al and an excess of octahedral cations (Table 2). Yet these chemical characteristics are inherent to the composition of the overall glauconitic packet, including the contaminating berthierine, not that of the pure glauconite/smectite structural units. Thus, the average crystal-chemical structural formula of interstratified glauconite-smectite is as follows:

$$(K_{0.23-0.57}Ca_{0.03-0.13}Na_{0-0.5})_{\Sigma 0.31-0.68}(Fe_{0.69-2.32}Mg_{0.19-0.54}Al_{0-0.74})_{\Sigma 2.05-2.79}(Si_{3.33-3.79}Al_{0.21-0.62}Fe_{0-0.29})_{\Sigma 4}O_{10}(OH)_2$$

In addition, the compositional variability seen for core 5 is plotted in the Fe-bearing clay phases diagram of Meunier and El Albani [18] (Figure 7a). The values fall within the

range of interlayer-deficient micas, ranging from the compositional domains of nontronite-berthierine towards glauconite-smectite. Similarly, the relationship between interlayer K^+ content (0.23-0.57 a.p.f.u.; Table 2) and expandable layer (% glauconite layers obtained by XRD: 35–75% $\pm$ 5%; Figure 5) in the interstratified glauconite-smectite mixed layer is presented in Figure 7b. These values were plotted against the calculated areal trend interpolation of López-Quirós et al. [62] after Baldermann et al. [13], based on values from different glaucony-bearing sequences. Glaucony pellets of core 5 are ascribed to a glauconite-smectite mixed layer composed of 35–75% glauconite layers and 65–25% of interstratified smectite layers.

Table 1. SEM-EDX microanalysis of the glaucony pellets (core 5) and glauconitic foraminiferal tests (selected surface samples) displaying the average K_2O, Fe_2O_3* (total) and Al_2O_3 values (wt %). * Total Fe expressed as Fe^{3+}. Min-max values in parentheses.

Sample	K_2O		Fe_2O_3*		Al_2O_3	
			Core 5 (HST)			
75 (n = 3)	3.4	(3.1–3.8)	19.8	(13.8–26.9)	5.3	(3.4–8)
99 (n = 9)	3.5	(2.9–4)	22.8	(18.5–27)	3.7	(2.7–4.7)
111 (n = 10)	3.7	(3.2–4.3)	22.9	(18.8–32.3)	3.5	(2.3–4.3)
119 (n = 11)	3.9	(3.3–4.7)	26	(20.6–37.2)	3.4	(1.9–4.2)
131 (n = 12)	3.7	(2.6–4.3)	22	(17.4–28.2)	4.1	(3.2–5.6)
139 (n = 12)	3.7	(3.1–5)	23.3	(14.3–29.8)	3.8	(2.9–6.2)
147 (n = 11)	3.9	(2.8–5.3)	24.5	(16.2–40.9)	3.7	(2.6–5.9)
159 (n = 9)	2.9	(1.7–3.9)	23.6	(19.1–29.7)	3.7	(2.8–4.2)
171 (n = 11)	3.3	(2.7–3.9)	29.1	(18.9–45.1)	3.3	(2.3–5)
			Surface samples (TST)			
A854 (n = 6)	4.5	(3.5–5.3)	29.5	(19.3–41.6)	3.5	(2.3–4.7)
A851 (n = 12)	4.5	(2–5.7)	24	(17.4–32.7)	3.9	(2.3–5.3)
A850 (n = 12)	4.8	(3.2–6.7)	20	(12–32.9)	5.2	(2.9–8.3)

Table 2. Results of AEM-calculated chemical analyses/structural formulae of glaucony pellets from core 5. [1] Units: atoms per formula unit (a.p.f.u.) based on $O_{10}(OH)_2$. * Total Fe expressed as Fe^{3+}. *M:* octahedrally coordinated cations; *A:* interlayer cations.

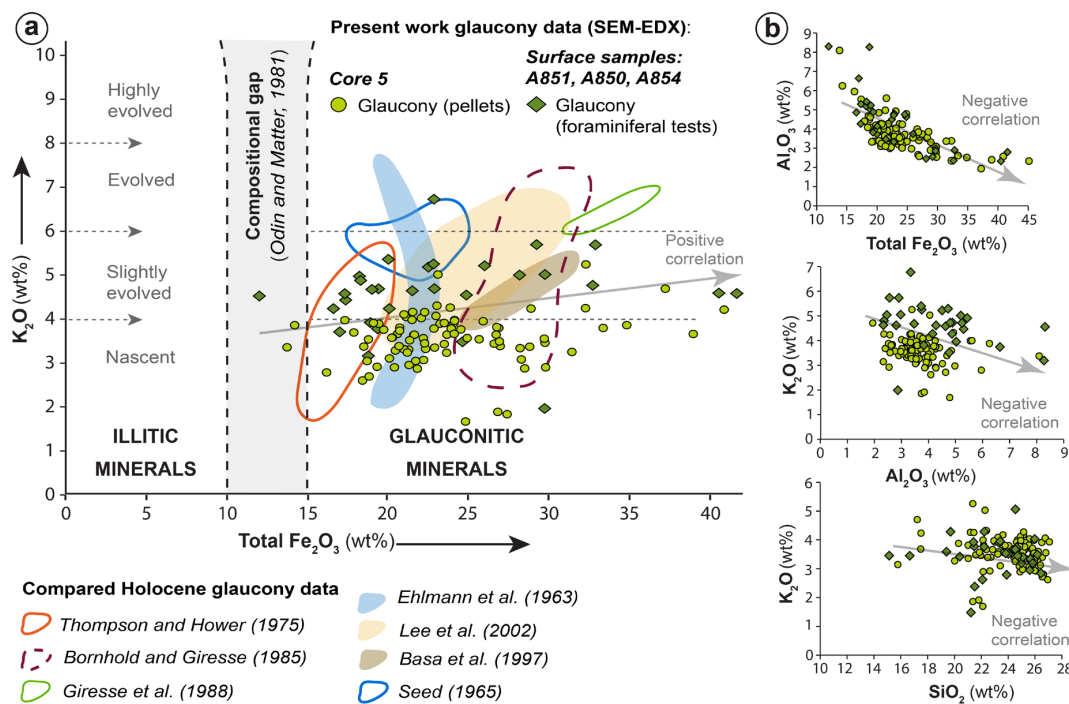| Sample	1	2	3	4	5	6	7	8	9	10	11	12	13	14	15	16	17
Si	3.6	3.54	3.51	3.57	3.5	3.79	3.6	3.41	3.46	3.59	3.55	3.55	3.36	3.52	3.41	3.38	3.33
^{IV}Al	0.24	0.46	0.41	0.43	0.31	0.21	0.4	0.38	0.54	0.25	0.45	0.45	0.64	0.24	0.59	0.62	0.38
Fe	0.16		0.08		0.19			0.21		0.16				0.24			0.29
Σ^{IV}	4	4	4	4	4	4	4	4	4	4	4	4	4	4	4	4	4
Ti	0	0	0	0	0	0	0	0	0	0	0	0	0	0	0	0	0
^{VI}Al	0	0.02	0	0.01	0	0.28	0.03	0	0.09	0	0.06	0.11	0.74	0	1.02	1.05	0
Fe*	1.66	1.65	1.7	1.65	1.68	1.9	2.32	1.63	1.59	1.68	1.6	1.57	0.94	1.63	0.69	0.92	1.75
Mg	0.47	0.42	0.41	0.42	0.44	0.49	0.44	0.54	0.47	0.37	0.47	0.4	0.42	0.48	0.4	0.19	0.49
$\Sigma^{VI}M$	2.13	2.09	2.11	2.08	2.12	2.67	2.79	2.17	2.15	2.05	2.13	2.08	2.1	2.11	2.11	2.16	2.24
Ca	0.05	0.06	0.06	0.04	0.05	0.05	0.13	0.11	0.11	0.05	0.05	0.04	0.06	0.05	0.05	0.03	0.04
Na	0.01	0.01	0.01	0	0.01	0.03	0	0.01	0	0.01	0.01	0.01	0.05	0.02	0.03	0.05	0
K	0.37	0.47	0.44	0.55	0.47	0.48	0.52	0.41	0.33	0.54	0.44	0.49	0.57	0.51	0.54	0.23	0.34
$\Sigma^{XII}A$	0.43	0.54	0.51	0.59	0.53	0.56	0.65	0.53	0.44	0.6	0.5	0.54	0.68	0.58	0.62	0.31	0.38

Figure 6. (**a**) Bivariate plot showing compositional relationships between K_2O vs. Fe_2O_3 (total Fe) derived from SEM-EDX microanalysis (Table 1). All data plot within the true glauconite field of Odin and Matter [17]. Values from different Holocene glaucony-bearing sequences are also plotted for comparison (Bornhold and Giresse [9], Thompson and Hower [63], Giresse et al. [64], Ehlmann et al. [65], Lee et al. [66], Basa et al. [67], Seed [68]). (**b**) Bivariate plots of Al_2O_3 vs. Fe_2O_3, K_2O vs. Al_2O_3 and K_2O vs. SiO_2, respectively.

Figure 7. (**a**) Projection of glaucony pellets (core 5) in the $M^+(Si/4)^{-1}$ vs. $^{VI}Fe/\Sigma^{VI}$ cations cross-plot (i.e., the Fe-bearing clay phases diagram of Meunier and El Albani [18]), representing the path of the glauconitization process from a nontronite-berthierine precursor. MLM: Mixed-layer minerals. (**b**) Relationship between % glauconite and interlayer K^+ (a.p.f.u.) content in the interstratified glauconite-smectite (Gl-Sm) mixed layers from core 5. Note that expandable layers (% glauconite ~35–75 ± 5) are determined by XRD, while interlayer K^+ (a.p.f.u.) content is from results of AEM (Table 2). Results are plotted against the calculated areal trend interpolation of López-Quirós et al. [62] after Baldermann et al. [13], based on values from different glaucony-bearing sequences.

4.2. Surface Samples: Glaucony from Exposed Transgressive Deposits

Glaucony grains recovered in the exposed transgressive sandy bulge (Figure 8a) occur as biogenic (mostly benthic foraminifera) casts and internal moulds, retaining the shape

of the original biogenic tests (Figure 8b–f). These grains show intermediate size, around 200–400 µm in diameter (Figure 8b–f). Glaucony grains display pale olive to green colours (Figure 8b–e) and smooth surfaces (Figure 8f) with moderate packing density and lamellar-flaky nanostructure (Figure 8g–i).
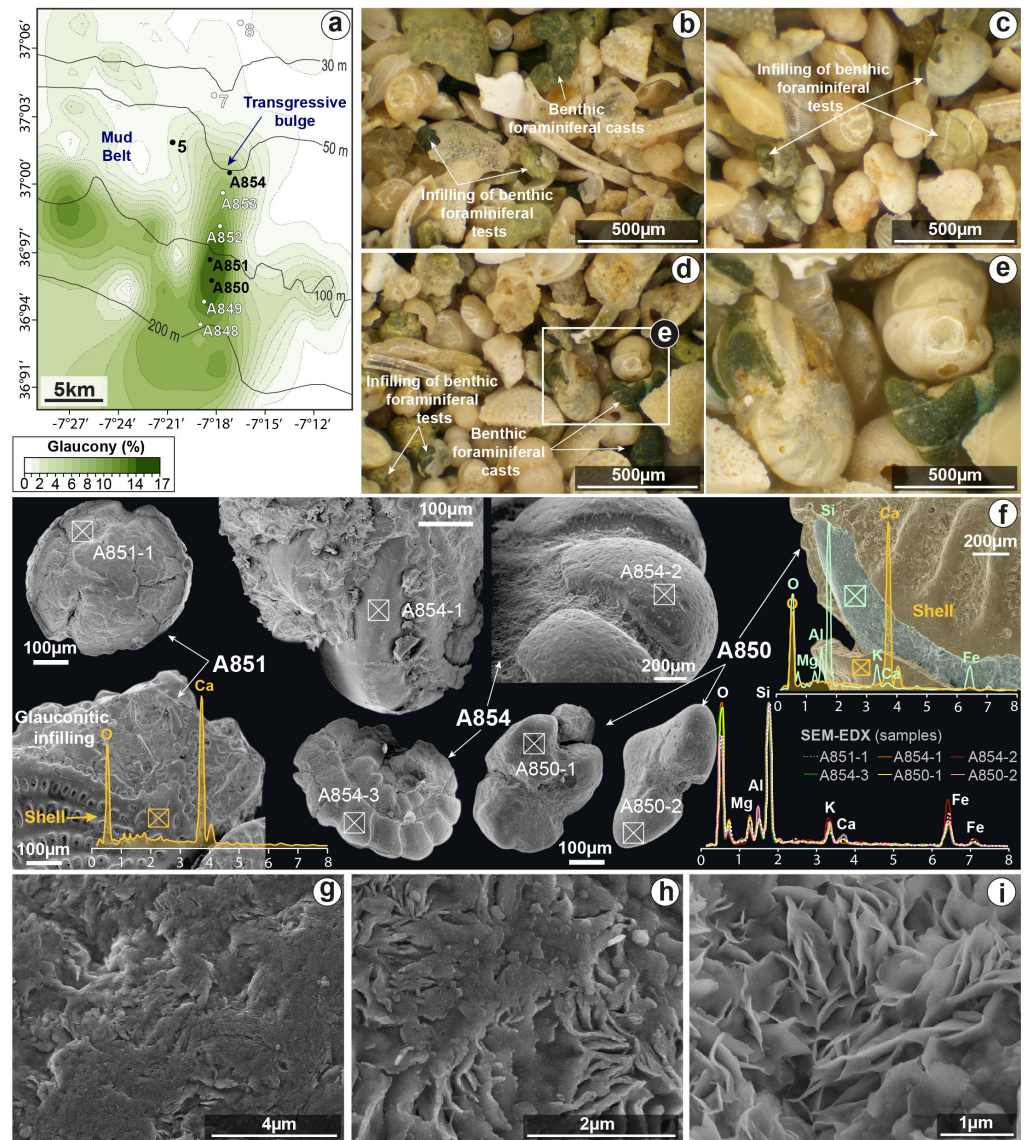

Figure 8. (**a**) Distribution map of glaucony-forming grains on the Guadiana shelf (from Gonzalez et al. [27]), with location of selected surface samples (A854, A853, A852, A851, A850, A849, and A848) from exposed transgressive deposits (i.e., the transgressive bulge). The location of core 5 in the vicinity of the mud belt is shown for comparison. (**b**–**e**), Digital photomicrographs showing the >63 µm size fraction of the glaucony-bearing muddy to sandy surface sediments. Glaucony occurs mainly as pale olive to green biogenic (benthic foraminifera) casts and internal moulds, retaining the shape of the original biogenic test. Other terrigenous components and microfossils such as non-glauconitized foraminifera are present. (**f**) SEM photomicrographs (SE) of sieved/purified glauconitic foraminiferal tests (casts/internal moulds) displaying smooth surfaces. Corresponding energy dispersive X-ray (EDX) analysis of each glauconitic test is shown. Furthermore, EDX analysis of foraminifera shells are also shown. (**g**–**i**), SEM photomicrographs (SE) showing moderate packing density lamellar-flaky nanostructure of glauconitic foraminiferal tests.

Glaucony from foraminiferal tests has mean concentrations of K_2O of 4.5–4.8 wt %, which are higher than the concentrations found in the glauconitized pellets from core 5

(Table 1 and Figure 7a). Fe_2O_3 contents range between 20–29.5 wt % (Table 1). Furthermore, K_2O appears to be positively correlated with Fe_2O_3 (Figure 6a). In contrast, Al_2O_3 contents are negatively correlated with Fe_2O_3 contents (Figure 6b). A negative correlation was also found between Al_2O_3 and K_2O, as well as with SiO_2 (Figure 6b).

In contrast to core 5, glaucony in transgressive deposits occurred through pseudomorphic replacement of foraminifera infillings as preferable substrate.

5. Discussion

5.1. The Glauconitization Process on the Guadiana Shelf

The most widely accepted model for the glauconitization process is the *'precipitation-dissolution-recrystallization theory'* [17,69], which includes two major evolutionary phases: (1) early diagenetic formation of a K-poor, Fe-rich glauconitic smectite (the Fe(III)-rich smectite precursor phase); and (2) the formation of K-rich glauconitic mica through chemical maturation (the Fe(III)-smectite-to-glauconite reaction) (e.g., see Figure 7 in López-Quirós et al. [70]). The results from the present study agree with this model.

Pellets, most likely a faecal product of invertebrate organisms based on their remaining morphology and internal texture [71], were the main substrate for the late Holocene (c. ~4.2–1.0 cal. ka BP) glauconitization event evidenced on the Guadiana Shelf. The pellets consist of a mixture of detrital clay particles, Fe-(oxy)hydroxides, K-feldspar, carbonates, and reactive organic matter, whereas their internal structure is relatively porous [72]. In sediment from core 5, faecal-pellet substrate provided an initially favourable organic-rich, semiconfined microsystem close to the sediment-water interface, with suitable early post-depositional conditions for the development of early glauconitic structures [10,13]. The occurrence of ill-defined globules and vermiform-like biomorphic nanostructures (Figure 3j), interpreted as bacterial remains in comparable glaucony-bearing sediments [70,73,74], may indicate that microbial activity played some role in the early glauconitization process, by oxidating organic matter within faecal pellets [15].

In sediments from core 5, winnowing would have stirred the mud fraction and led to sub-oxygenation. The oxidation of organic matter most probably promoted dissolution of detrital silicates (feldspar and clay minerals; [13,14]), Fe-(oxy)hydroxides, and carbonates under local, partially reducing and slightly acidic conditions (for a recent review, see López-Quirós et al. [62] and Giresse [75]). Accordingly, mobile Fe (Fe^{2+}) and other elements such as Si, Al, or Ca, were released by reductive dissolution reactions into interstadial fluids and surrounding seawater [15]. Moreover, ferruginous seawater enriched in Fe^{2+} at the sediment-water interface is also available in upwelling systems [76–79]. This particular situation promoted a reservoir of free ions in solution for the early formation of the Fe(III)-smectite precursor within the pores of faecal pellets at our study site (a very early diagenetic process lasting $10–10^3$ years; [13]). The Fe(III)-smectite precursor may have precipitated from a gel-like substance as previously reported [13,80–82]. In the studied core, the presence of 7Å–phase relics (Figure 4c–f) suggests that formation of the Fe(III)-rich smectite precursor preceded or coexisted with an intermediate trioctahedral (berthierine) phase. Fe(III)-smectite (nontronite) associated with berthierine was thus the most likely precursor mineral to glauconitization of faecal pellets on the Guadiana shelf (Figure 7a).

Once mobilized under moderately reducing conditions, Fe^{2+} may have migrated into the faecal pellets where it was partly oxidized to Fe^{3+}, possibly mediated by the mineralization of organic matter and cessation of microbial reactions, and then stabilized in the octahedral sheet of the Fe(III)-smectite precursor [15,18,81]. With advanced shallow (early) diagenesis, the neo-formed Fe(III)-smectite would have become thermodynamically unstable [81] and transformed into glauconite crystals throughout the formation of inter-stratified glauconite-smectite mixed-layer minerals (i.e., a diffusion-controlled reaction; [18]) (Figure 7b). On the Guadiana shelf, faecal pellets would have been partially reducing microenvironments in contrast to the oxidizing conditions in the enclosing sediment. This would have provided the redox conditions needed to promote the smectite-to-glauconite reaction [10,11,13,15,22,23,62,70,75,83].

Average K_2O content is largely used as an indicator for assessing the evolution (maturity) of the smectite-to-glauconite reaction, because progressive fixation of K^+ has a strong influence on the evolution of the glaucony-forming process [7,10,17,62,75]. Immature (nascent) glaucony occurs in core 5 (e.g., Figures 3i,j, 5 and 6a), but most glaucony pellets reached a slightly evolved stage, with mean K_2O values around 4% (Figure 6a and Table 1). The dominant occurrence of glaucony in a slightly evolved mature stage (Figure 6a) indicates that faecal pellets underwent a limited period of residence at the sediment–water interface before burial. During glaucony maturation, a gradually higher octahedral charge deficiency develops due to the reduction of $Fe(III)$ to $Fe(II)$, K^+ uptake into the interlayer sites increase, and the proportion of expandable smectite layers in the interstratified glauconite-smectite decreases [62]. Chemical maturity correlates with the neo-formation of multiple microcrystallites (flakes) infilling the intra-grain porosity. The growth of Fe-smectite and interlayered clay flakes produces variations in density (between the parent mud and the successive glaucony evolutionary phases) [23,75]. In core 5, neo-formation of hydrated minerals likely triggered a decrease in packing size/density, hence an increase in grain volume, favouring cracking at the pellet surface (Figure 3h). These morpho-textural features can be attributed to a slightly evolved mature stage of glaucony grains on the Guadiana shelf. These poorly evolved to evolved nanostructures (Figures 3i–n and 4a) together with the moderate % of mica layers (35–75; Figures 5 and 7b) present in the interstratified glauconite-smectite is consistent with the glauconitization process on the Guadiana shelf being halted at an early stage.

5.2. Glaucony in a Sequence-Stratigraphic Framework

5.2.1. Autochthonous versus Allochthonous Origin

The distinction between in situ (autochthonous) and allochthonous (reworked) glaucony occurrences, with further subdivision of the latter in detrital (extra-sequential) and parautochthonous (intra-sequential), is required for reliable interpretations of glaucony-bearing sections and their application in a sequence stratigraphic context [1,7,84–87]. As is widely accepted, glaucony grains with an autochthonous origin are linked to the TST and the lower HST [1,7,10,11,17–19,21,88]. A revised conceptual model on glaucony distribution recognised an overall upward-increasing trend in abundance and maturity of glaucony grains in the TST, followed by a rapid decreasing trend in the lower part of the overlying HST, the maximum concentration of evolved glaucony grains being associated with the TST/HST Maximum Flooding Surface boundary. Such an evolution is related principally to variations in sediment supply, which occur in response to the changing rate of relative eustatic sea-level rise [7].

It has been shown, however, that both penecontemporaneous remobilization of intra-sequential glaucony and reworking of extra-sequential glaucony are very likely to lead to large concentrations of allochthonous glaucony at stratigraphic levels other than those traditionally postulated [1,84–87]. Remobilization of parautochthonous glaucony is mainly linked to wave-, tide-, and storm-dominated deposits within the TST and HST, where glaucony tends to show low concentrations and low to moderate maturity [1,7]. In turn, reworking of extra-sequential glaucony is usually linked to subaerial exposure during lowstands.

On the Guadiana shelf, late Holocene glaucony grains deposited during advanced highstand conditions are interpreted as formed in situ and not affected by significant physical transport processes or intense bioturbation. The first indication of the autochthonous glaucony origin is the low thickness (<1 m) of the glaucony-bearing condensed section (Figure 2a). Moreover, preservation patterns of benthic foraminifera coexisting with glauconitized pellets indicate no significant sediment reworking, given the authigenic precipitation of the carbonates [29]. Another reliable signal of authigenesis is the scarcity of small fragments of broken glaucony grains and the occurrence of poorly evolved radial cracks within these grains (Figure 3b–h). This pattern denotes a slight (or no) mechanical breakdown. Therefore, remobilization of glauconitic grains from transgressive glaucony-bearing sections into overlying highstand deposits is ruled out. Glauconitization during the

transgressive phase occurred largely through pseudo-morphic replacement of foraminifera infillings as preferable substrate (Figure 8b–f). In contrast, only glauconitized faecal pellets were found in the highstand deposits, hence the glaucony from the underlying transgressive phase was not reworked into the younger sediments.

5.2.2. Factors Influencing the (Bio)availability of Fe during Highstand Conditions

The radiocarbon age for glauconitization in core 5 (c. 4.2–1.0 cal. ka BP, according to Mendes et al., [29]) is considerably younger than the initiation of the Holocene highstand in the region at about 6.5 ka (e.g., [44]), during which quite stable climatic and environmental conditions are interpreted [29]. Major highstand deposition is usually accompanied by a basin-ward shift of coastal and marginal marine facies, as sediment accumulation rates exceed the rate of creation of accommodation space. Highstands would thus be hostile for the glauconitization process, since glaucony authigenesis depends largely on reduced sedimentation rates to promote—as discussed above (Section 5.1)—the incorporation of Fe and subsequently K, and especially on the rate of aqueous Fe^{2+} diffusion. Therefore, a combination of factors must be invoked to explain the peak in glaucony abundance during typical highstand conditions postdating the period of maximum shelf flooding.

The middle shelf sediment, from which the core was retrieved, was characterized by temporally changing sedimentation rates, with low sedimentation rates for at least about 4.5 ka (from 4.17 to 0.72 cm/ka BP; Figure 2a), and subsequent increases to 117.5 cm/ka BP (Figure 2a) driven by climatic anomalies and by human activities such as mining and agriculture [3,29,47]. Accordingly, sedimentation rates on the Guadiana Shelf during advanced highstand conditions were low enough (~17.5 cm/ka; Figure 2a) for the Fe-rich smectite precursor of glauconite to form. Such favourable conditions did not necessarily exist during the final sea-level rise predating the Holocene highstand. Indeed, during MWP-1B, characterized by high rates of sea-level rise, phases of enhanced deltaic sedimentation have been documented in the study area [28].

Another factor to be taken into account for the initial precipitation of Fe-rich smectite is the abundance and (bio)availability of Fe (Fe^{2+}). Normal seawater usually contains very low concentrations of Fe, not providing the necessary conditions for glauconitization. Hence, a continental weathering-related supply of Fe will favour glauconitization in shallow marine sediments [27,89]. A further source for glaucony authigenesis is the supply of nutrient (Fe)-rich waters to the shelf (e.g., [90]) will similarly favour glauconitization. In modern oceans, Fe is available in nutrient-rich upwelling zones in shelf-to-slope environments where the occurrence of glaucony is often reported [76–79].

We propose that in the study area, Fe availability was promoted by a succession of marine and continental processes that took place under protracted conditions of low sedimentation rates on the shelf. During c. 4.4–4.0 cal. ka BP, reported evidence indicates that a strong nutrient-rich upwelling system was established in the whole region of the Gulf of Cadiz [91], in agreement with the major glaucony abundance in core 5 (Figure 3a). Increased productivity related to enhanced upwelling during the middle-late Holocene is consistent with reported marked faunal (benthic foraminifera) changes (Figure 2a; [55]) and with a greater supply of fine-sized marine organic matter (Figure 2a; [47]). The established upwelling system was probably not associated with wind-driven processes prevailing in the coastal region, but more likely with an eastward extension of the Azores Front, which is characterized by locally intense upwelling along the Azores Current entering the Gulf of Cadiz [91]. In contrast, the study area is influenced at present by the eastward distribution of seasonal upwelling occurring off Cape Santa Maria, generating a filament that extends to the Guadiana Shelf [92,93].

After 4 ka, episodes of marked aridity, together with anthropogenic-derived weathering of the landscape during the protohistoric period, from c. 2.5 to 1.0 cal. ka BP, possibly caused a flux of Fe-enriched terrigenous particles to the Guadiana River basin (e.g., [52,94]). At the site of core 5, this period coincides with the upper glaucony-bearing interval and cessation of glaucony authigenesis (Figure 3a). In this context, ore mining and metal pro-

cessing activities related to the Roman occupation of SW Iberia contributed to the dispersal of metals in the continental shelf, including the supply of Fe [57,58].

Taking into account all the above considerations, we estimate that the high (~20–29 wt %) total Fe (Fe_2O_3 + FeO) content of late Holocene glaucony occurrences in the studied sediment core could be a consequence of a combination of ferruginous-rich upwelling waters and latterly of natural to anthropogenic land-derived (weathering) supply, which triggered a rise of Fe content in the seawater.

6. Conclusions

Detailed morpho-textural, mineralogical, and geochemical analyses of green clays (glaucony grains) provide new insights to understand early glauconization processes and to unravel palaeo-environmental conditions during the Holocene that were favourable for glaucony development in shallow-water settings, specifically focusing on the transgressive versus highstand dichotomy. Our combined dataset supports the occurrence of two phases of glauconitization in the study area: the first would be related to postglacial transgression, and the second to late Holocene highstand conditions.

On the Guadiana shelf, conditions for the late Holocene glauconitization of faecal pellets in an open shelf-environment (~70 m) occurred as a result of low sedimentation rates, high Fe flux and suboxic, partially reducing conditions near the sediment-water interface. Suboxic conditions prevailed in the surrounding substrate owing to periodic winnowing action, which in turn slightly stirred the mud fraction, enhancing the concentration of pellets. Glaucony grains in a slightly evolved mature stage further reveal that pellets capable of glauconitization underwent a limited period of residence at the sediment-water interface before sediment burial.

Contrary to predictions made in the light of traditional sequence-stratigraphic models, this study demonstrates that autochthonous glaucony grains formed at the middle to upper HST, as (bio)availability of Fe was not a limiting factor for glaucony authigenesis during such highstand conditions. On the middle shelf, iron required for the glaucony-forming process was supplied by a combination of nutrient-rich upwelling waters and the alteration of continent-derived minerals. Both the marine and continental processes took place during protracted intervals of low sedimentation rates on the Guadiana Shelf.

References

1. Amorosi, A. Glaucony and sequence stratigraphy: A conceptual framework of distribution in siliciclastic sequences. *J. Sediment. Res.* **1995**, *B65*, 419–425.
2. Stonecipher, S.A. Genetic characteristic of glauconite and siderite: Implications for the origin of ambiguous isolated marine sandbodies. In *Isolated Shallow Marine Sand Bodies: Sequence Stratigraphic Analysis and Sedimentological Interpretation*; Bergman, K.M., Snedden, J.W., Eds.; SEPM Special Publications: Broken Arrow, OK, USA, 1999; Volume 64, pp. 191–204.
3. Morad, S.; Ketzer, J.M.; De Ros, F. Spatial and temporal distribution of diagenetic alterations in siliciclastic rocks: Implications for mass transfer in sedimentary basins. *Sedimentology* **2000**, *47*, 95–120. [CrossRef]
4. Taylor, K.G.; Macquaker, J.H.S. Spatial and temporal distribution of authigenic minerals in continental shelf sediments: Implications for sequence stratigraphic analysis. In *Marine Authigenesis: From Globial to Microbial*; Glenn, C.R., Prevot-Lucas, L., Lucas, J., Eds.; SEPM Special Publications: Broken Arrow, OK, USA, 2000; Volume 66, pp. 309–323.
5. Ketzer, J.M.; Holz, M.; Morad, S.; Al-Aasm, I.S. Sequence stratigraphic distribution of diagenetic alterations in coal-bearing, paralic sandstones: Evidence from the Rio Bonito Formation (Early Permian), southern Brazil. *Sedimentology* **2003**, *50*, 855–877. [CrossRef]
6. Al-Ramadan, K.; Morad, S.; Proust, J.N.; Al-Aasm, I. Distribution of diagenetic alterations in siliciclastic shoreface deposits within a sequence stratigraphic framework: Evidence from the Upper Jurassic, Boulonnais, NW France. *J. Sediment. Res.* **2005**, *75*, 943–959. [CrossRef]
7. Amorosi, A. The occurrence of glaucony in the stratigraphic record: Distribution patterns and sequence stratigraphic significance. *Int. Assoc. Sedimentol. Spec. Publ.* **2012**, *45*, 37–54.
8. Huggett, J.M. *Minerals: Glauconites and Green Clays, Reference Module in Earth Systems and Environmental Sciences*; Elsevier: Amsterdam, The Netherlands, 2013.
9. Bornhold, B.D.; Giresse, P. Glauconitic sediments on the continental shelf off Vancouver Island, British Columbia, Canada. *J. Sediment. Petrol.* **1985**, *55*, 653–664.
10. Odin, G.S. Green Marine Clays. In *Develop Sediment 45*; Elsevier: Amsterdam, The Netherlands, 1988; p. 444.
11. Giresse, P.; Wiewiora, A. Stratigraphic condensed deposition and diagenetic evolution of green clay minerals in deep water sediments on the Ivory Coast-Ghana Ridge. *Mar. Geol.* **2001**, *179*, 51–70. [CrossRef]
12. Cuadros, J.; Dekov, V.M.; Arroyo, X.; Nieto, F. Smectite formation in submarine hydrothermal sediments: Samples from the HMS Challenger Expedition (1872–1776). *Clays Clay Miner.* **2011**, *59*, 147–164. [CrossRef]
13. Baldermann, A.; Warr, L.N.; Grathoff, G.H.; Dietzel, M. The rate and mechanism of deep-sea glauconite formation at the Ivory Coast-Ghana Marginal Ridge. *Clays Clay Miner.* **2013**, *61*, 258–276. [CrossRef]
14. El Albani, A.; Meunier, A.; Fürsich, F. Unusual occurrence of glauconite in a shallow lagoonal environment (Lower Cretaceous, northern Aquitaine Basin, SW France). *Terra Nova* **2005**, *17*, 537–544. [CrossRef]
15. Baldermann, A.; Grathoff, G.H.; Nickel, C. Micromilieu-controlled glauconitization in fecal pellets at Oker (Central Germany). *Clay Miner.* **2012**, *47*, 513–538. [CrossRef]
16. Huggett, J.M.; Cuadros, J. Glauconite formation in lacustrine/palaeosol sediments, Isle of Wight (Hampshire Basin), UK. *Clay Miner.* **2010**, *45*, 35–49. [CrossRef]
17. Odin, G.S.; Matter, A. De glauconiarum origine. *Sedimentology* **1981**, *28*, 611–641. [CrossRef]
18. Meunier, A.; El Albani, A. The glauconite-Fe-illite-Fe-smectite problem: A critical review. *Terra Nova* **2007**, *19*, 95–104. [CrossRef]
19. Banerjee, S.; Bansal, U.; Thorat, A. A review on palaeogeographic implications and temporal variation in glaucony composition. *J. Paleogeogr.* **2016**, *5*, 43–71. [CrossRef]
20. Rudmin, M.; Banerjee, S.; Mazurov, A. Compositional variation of glauconites in Upper Cretaceous-Paleogene sedimentary iron-ore deposits in South-eastern Western Siberia. *Sediment. Geol.* **2017**, *355*, 20–30. [CrossRef]
21. López-Quirós, A.; Escutia, C.; Etourneau, J.; Rodríguez-Tovar, F.J.; Roignant, S.; Lobo, F.J.; Thompson, N.; Bijl, P.K.; Bohoyo, F.; Salzmann, U.; et al. Eocene-Oligocene paleoenvironmental changes in the South Orkney Microcontinent (Antarctica) linked to the opening of Powell Basin. *Glob. Planet. Change* **2021**, *204*, 103581. [CrossRef]
22. Wiewióra, A.; Giresse, P.; Petit, S.; Wilamowski, A. A deep-water glauconitization process on the Ivory Coast–Ghana Marginal Ridge (ODP site 959): Determination of Fe3+-rich montmorillonite in green grains. *Clays Clay Miner.* **2001**, *49*, 540–558. [CrossRef]
23. Giresse, P. Chapter 12 some aspects of diagenesis in contourites. In *Developments in Sedimentology*; Rebesco, M., Camerlenghi, A., Eds.; Elsevier: Amsterdam, The Netherlands, 2008; pp. 203–221.
24. Lobo, F.J.; Hernández-Molina, F.J.; Somoza, L.; Díaz del Río, V. The sedimentary record of the post-glacial transgression on the Gulf of Cadiz continental shelf (Southwest Spain). *Mar. Geol.* **2001**, *178*, 171–195. [CrossRef]
25. Lobo, F.J.; Sánchez, R.; González, R.; Dias, J.M.A.; Hernandez-Molina, F.J.; Fernández-Salas, L.M.; Díaz del Río, V.; Mendes, I. Contrasting styles of the Holocene highstand sedimentation and sediment dispersal systems in the northern shelf of the Gulf of Cadiz. *Cont. Shelf Res.* **2004**, *24*, 461–482. [CrossRef]
26. Lobo, F.J.; Ridente, D. Stratigraphic architecture and spatio-temporal variability of high-frequency (Milankovitch) depositional cycles on modern continental margins: An overview. *Mar. Geol.* **2014**, *352*, 215–247. [CrossRef]
27. Gonzalez, R.; Dias, J.M.A.; Lobo, F.; Mendes, I. Sedimentological and paleoenvironmental characterisation of transgressive sediments on the Guadiana Shelf (Northern Gulf of Cadiz, SW Iberia). *Quat. Int.* **2004**, *120*, 133–144. [CrossRef]

28. Carrión-Torrente, A.; Lobo, F.J.; Puga-Bernabéu, A.; Mendes, I.; Lebreiro, S.; Garcia, M.; van Rooij, D.; Lujan, M.; Reguera, M.I.; Antón, L. Episodic postglacial deltaic pulses in the Gulf of Cadiz: Implications for the development of a transgressive shelf and driving environmental conditions. *J. Sediment. Res.* **2022**, *92*, 1–25. [CrossRef]

29. Mendes, I.; Dias, J.A.; Schönfeld, J.; Ferreira, Ó.; Rosa, F.; Gonzalez, R.; Lobo, F.J. Natural and human-induced Holocene paleoenvironmental changes, on the Guadiana shelf (northern Gulf of Cadiz). *Holocene* **2012**, *22*, 1011–1024. [CrossRef]

30. Hanebuth, T.J.J.; King, M.L.; Lobo, F.J.; Mendes, I. Formation history and material budget of holocene shelf mud depocenters in the Gulf of Cadiz. *Sediment. Geol.* **2021**, *421*, 105956. [CrossRef]

31. Loureiro, J.J.M.; Nunes, M.N.F.; Machado, M.L.R. A Bacia Hidrográfica do Rio Guadiana. In *Monografias Hidrológicas dos Principais Cursos de Água de Portugal Continental*; Direcção Geral dos Recursos e Aproveitamentos: Lisboa, Portugal, 1986; pp. 341–407.

32. Mendes, I.; Lobo, F.J.; Hanebuth, T.J.J.; López-Quirós, A.; Schönfeld, J.; Lebreiro, S.; Reguera, M.I.; Antón, L.; Ferreira, Ó. Temporal variability of flooding events of Guadiana River (Iberian Peninsula) during the middle to late Holocene: Imprints in the shallow-marine sediment record. *Palaeogeogr. Palaeoclimatol. Palaeoecol.* **2020**, *556*, 109900. [CrossRef]

33. Morales, J.A. Evolution and facies architecture of the mesotidal Guadiana River delta (S.W. Spain-Portugal). *Mar. Geol.* **1997**, *138*, 127–148. [CrossRef]

34. Portela, L.I. Sediment Delivery from the Guadiana Estuary to the Coastal Ocean. *J. Coast. Res.* **2006**, *39*, 1819–1823.

35. Gonzalez, R.; Dias, J.A.; Ferreira, Ó. Recent rapid evolution of the Guadiana estuary (south western Iberian Peninsula). *J. Coast. Res. SI* **2001**, *34*, 516–527.

36. Nelson, C.H.; Baraza, J.; Maldonado, A.; Rodero, J.; Escutia, C.; Barber, J.H. Influence of the Atlantic inflow and Mediterranean outflow currents on Late Quaternary sedimentary facies of the Gulf of Cadiz continental margin. *Mar. Geol.* **1999**, *155*, 99–129. [CrossRef]

37. García-Lafuente, J.; Delgado, J.; Criado-Aldeanueva, F.; Bruno, M.; del Río, J.; Miguel Vargas, J. Water mass circulation on the continental shelf of the Gulf of Cádiz. *Deep Sea Res. Part II Top. Stud. Oceanogr.* **2006**, *53*, 1182–1197. [CrossRef]

38. Ruiz, J.; Navarro, G. Upwelling spots and vertical velocities in the Gulf of Cádiz: An approach for their diagnose by combining temperature and ocean colour remote sensing. *Deep Sea Res. Part II Top. Stud. Oceanogr.* **2006**, *53*, 1282–1293. [CrossRef]

39. De Oliveira Júnior, L.; Garel, E.; Relvas, P. The structure of incipient coastal counter currents in South Portugal as indicator of their forcing agents. *J. Mar. Syst.* **2021**, *214*, 103486. [CrossRef]

40. Prieto, L.; Navarro, G.; Rodríguez-Gálvez, S.; Huertas, I.E.; Naranjo, J.M.; Ruiz, J. Oceanographic and meteorological forcing of the pelagic ecosystem on the Gulf of Cadiz shelf (SW Iberian Peninsula). *Cont. Shelf Res.* **2009**, *29*, 2122–2137. [CrossRef]

41. Criado-Aldeanueva, F.; García-Lafuente, J.; Vargas, J.M.; Del Río, J.; Vázquez, A.; Reul, A.; Sánchez, A. Distribution and circulation of water masses in the Gulf of Cádiz from in situ observations. *Deep. Sea Res. II* **2006**, *53*, 1144–1160. [CrossRef]

42. Garel, E.; Laiz, I.; Drago, T.; Relvas, P. Characterisation of coastal counter-currents on the inner shelf of the Gulf of Cadiz. *J. Mar. Syst.* **2016**, *155*, 19–34. [CrossRef]

43. Bellanco, M.J.; Sánchez-Leal, R.F. Spatial distribution and intra-annual variability of water masses on the Eastern Gulf of Cadiz seabed. *Cont. Shelf Res.* **2016**, *128*, 26–35. [CrossRef]

44. Zazo, C.; Goy, J.L.; Somoza, L.; Dabrio, C.J.; Belluomini, G.; Improta, S.; Lario, J.; Bardaji, T.; Silva, P.G. Holocene sequence of sea-level fluctuations in relation to climatic trends in the Atlantic–Mediterranean linkage coast. *J. Coast. Res.* **1994**, *10*, 933–945.

45. Gutiérrez-Mas, J.M.; Hernández-Molina, F.J.; López Aguayo, F. Holocene sedimentary dynamics on the Iberian continental shelf of the Gulf of Cadiz (SW Spain). *Cont. Shelf Res.* **1996**, *16*, 1635–1653. [CrossRef]

46. Lobo, F.J.; Mendes, I.; García, M.; Reguera, M.I.; Antón, L.; Lebreiro, S.L.; Van Rooij, D.; Luján, M.; Fernández-Puga, M.C.; Dias, J.M.A. A progradational pulse during the initial postglacial shelf drowning in the northern Gulf of Cadiz. In *8° Simposio del Margen Continental Ibérico Atlántico, Abstract Volume*; Díaz del Río, V., Bárcenas, P., Fernández-Salas, L.M., López-González, N., Palomino, D., Rueda, J.L., Sánchez-Guillamón, O., Vázquez, J.T., Eds.; Sia Graf: Malaga, Spain, 2015; pp. 619–622.

47. Burdloff, D.; Araújo, M.F.; Jouanneau, J.-M.; Mendes, I.; Monge Soares, A.M.; Dias, J.M.A. Sources of organic carbon in the Portuguese continental shelf sediments during the Holocene period. *Appl. Geochem.* **2008**, *23*, 2857–2870. [CrossRef]

48. Boski, T.; Moura, D.; Veiga-Pires, C.; Camacho, S.; Duarte, D.; Scott, D.B.; Fernandes, S.G. Postglacial sea-level rise and sedimentary response in the Guadiana Estuary, Portugal/Spain border. *Sediment. Geol.* **2002**, *150*, 103–122. [CrossRef]

49. Goy, J.L.; Zazo, C.; Dabrio, C.J.; Lario, J.; Borja, F.; Sierro, F.J.; Flores, J.A. Global and regional factors controlling changes of coastlines in southern Iberia (Spain) during the Holocene. *Quat. Sci. Rev.* **1996**, *15*, 773–780. [CrossRef]

50. Boski, T.; Camacho, S.; Moura, D.; Fletcher, W.; Wilamowski, A.; Veiga-Pires, C.; Correia, V.; Loureiro, C.; Santana, P. Chronology of the sedimentary processes during the postglacial sea level rise in two estuaries of the Algarve coast, Southern Portugal. *Estuar. Coast. Shelf Sci.* **2008**, *77*, 230–244. [CrossRef]

51. Delgado, J.; Boski, T.; Nieto, J.M.; Pereira, L.; Moura, D.; Gomes, A.; Sousa, C.; García-Tenorio, R. Sea-level rise and anthropogenic activities recorded in the late Pleistocene/Holocene sedimentary infill of the Guadiana Estuary (SW Iberia). *Quat. Sci. Rev.* **2012**, *33*, 121–141. [CrossRef]

52. Fletcher, W.J.; Boski, T.; Moura, D. Palynological evidence for environmental and climatic change in the lower Guadiana valley, Portugal, during the last 13,000 years. *Holocene* **2007**, *17*, 481–494. [CrossRef]

53. Chester, D.K.; James, P.A. Late Pleistocene and Holocene landscape development in the Algarve Region, Southern Portugal. *J. Mediterr. Archaeol.* **1999**, *12*, 169–196. [CrossRef]

54. Boone, J.L.; Worman, F.S. Rural settlement and soil erosion from the late Roman Period through the medieval Islamic Period in the lower Alentejo of Portugal. *J. Field Archaeol.* **2007**, *32*, 115–132. [CrossRef]

55. Mendes, I.; Dias, J.A.; Schönfeld, J.; Ferreira, Ó.; Rosa, F.; Lobo, F.J. Living, dead and fossil benthic foraminifera on a river dominated shelf (northern Gulf of Cadiz) and their use for paleoenvironmental reconstruction. *Cont. Shelf Res.* **2013**, *68*, 91–111. [CrossRef]

56. Mil-Homens, M.; Vale, C.; Naughton, F.; Brito, P.; Drago, T.; Anes, B.; Raimundo, J.; Schmidt, S.; Caetano, M. Footprint of roman and modern mining activities in a sediment core from the southwestern Iberian Atlantic shelf. *Sci. Total Environ.* **2016**, *571*, 1211–1221. [CrossRef]

57. Mil-Homens, M.; Vale, C.; Brito, P.; Naughton, F.; Drago, T.; Raimundo, J.; Anes, B.; Schmidt, S.; Caetano, M. Insights of Pb isotopic signature into the historical evolution and sources of Pb contamination in a sediment core of the southwestern Iberian Atlantic shelf. *Sci. Total Environ.* **2017**, *586*, 473–484. [CrossRef]

58. Hanebuth, T.J.J.; King, M.L.; Mendes, I.; Lebreiro, S.; Lobo, F.J.; Oberle, F.K.J.; Antón, L.; Ferreira, P.A.; Reguera, M.I. Hazard potential of widespread but hidden historic offshore heavy metal (Pb, Zn) contamination (Gulf of Cadiz, Spain). *Science of the Total Environ.* **2018**, *637–638*, 561–576. [CrossRef] [PubMed]

59. Lorimer, G.W.; Cliff, G. Analytical electron microscopy of minerals. In *Electron Microscopy in Mineralogy*; Wenk, H.-R., Ed.; Springer: Berlin/Heidelberg, Germany, 1976; pp. 506–519.

60. Buatier, M.; Honnorez, J.; Ehret, G. Fe-smectite-glauconite transition in hydrothermal green clays from the Galapagos spreading center. *Clays Clay Miner.* **1989**, *37*, 532–541. [CrossRef]

61. Moore, D.M.; Reynolds, R.C. *X-ray Diffraction and the Identification and Analysis of Clay Minerals*, 2nd ed.; Oxford University Press: Oxford, UK, 1997; p. 378.

62. López-Quirós, A.; Sánchez-Navas, A.; Nieto, F.; Escutia, C. New insights into the nature of glauconite. *Am. Mineral.* **2020**, *105*, 674–686. [CrossRef]

63. Thompson, G.R.; Hower, J. 1975. The mineralogy of glauconite. *Clays Clay Miner.* **1975**, *23*, 289–300. [CrossRef]

64. Giresse, P.; Wiewiora, A.; Lacka, B. Mineral phases and processes within green peloids from two recent deposits near the Congo River Mouth. *Clay Miner.* **1988**, *23*, 447–458. [CrossRef]

65. Ehlmann, A.; Hulings, N.; Glover, E. Stages of glauconite formation in modern foraminiferal sediments. *J. Sediment. Petrol.* **1963**, *33*, 87–96.

66. Lee, C.H.; Choi, S.; Suh, M. High iron glaucony from the continental shelf of the Yellow Sea off the southwestern Korean Peninsula. *J. Asian Earth Sci.* **2002**, *20*, 507–515. [CrossRef]

67. Basa, T.; Greensmith, J.T.; Finzi, C.V. The sub-surface Holocene Middle sands of Dungeness. *Proc. Geol. Assoc.* **1997**, *108*, 105–112. [CrossRef]

68. Seed, D.P. The formation of vermicular pellets in New Zealand glauconites. *Am. Mineral.* **1965**, *50*, 1097–1106.

69. Odin, G.S.; Fullagar, P.D. Geological significance of the glaucony facies. *Green Mar. Clays* **1988**, *45*, 295–332.

70. López-Quirós, A.; Escutia, C.; Sánchez-Navas, A.; Nieto, F.; García-Casco, A.; Martín-Algarra, A.; Evangelinos, D.; Salabarnada, A. Glaucony authigenesis, maturity and alteration in the Weddell Sea: An indicator of paleoenvironmental conditions before the onset of Antarctic glaciation. *Sci. Rep.* **2019**, *9*, 13580. [CrossRef] [PubMed]

71. McRae, S.G. Glauconite. *Earth Sci. Rev.* **1972**, *8*, 397–440. [CrossRef]

72. Pilskaln, C.H.; Honjo, S. The fecal pellet fraction of biogeochemical particle fluxes to the deep sea. *Glob. Biogeochem. Cycles* **1987**, *1*, 31–48. [CrossRef]

73. Zanin, Y.N.; Eder, V.G.; Zamirailova, A.G. Bacterial forms in glauconites from Upper Jurassic deposits of the West Siberian Plate. *Russ. Geol. Geophys.* **2004**, *45*, 774–777.

74. Eder, V.G.; Martin-Algarra, A.; Sanchez-Navas, A.; Zanin, Y.N.; Zamiralova, A.G.; Lebedev, Y.N. Depositional controls on glaucony texture and composition, Upper Jurassic, West Siberian Basin. *Sedimentology* **2007**, *54*, 1365–1387. [CrossRef]

75. Giresse, P. Quaternary Glauconitization on Gulf of Guinea, Glauconite Factory: Overview of and New Data on Tropical Atlantic Continental Shelves and Deep Slopes. *Minerals* **2022**, *12*, 908. [CrossRef]

76. Cook, P.J.; Marshall, J.F. Geochemistry of iron and phosphorus-rich nodules from the east Australian continental shelf. *Mar. Geol.* **1981**, *41*, 205–221. [CrossRef]

77. Glenn, C.R.; Arthur, M.A. Anatomy and origin of a Cretaceous phosphorite-greensand giant, Egypt. *Sedimentology* **1990**, *37*, 123–154. [CrossRef]

78. Glenn, C.R.; Föllmi, K.B.; Riggs, S.R.; Baturin, G.N.; Grimm, K.A.; Trappe, J.; Abed, A.M.; Galli-Oliver, C.; Garrison, R.E.; Ilyan, A.; et al. Phosphorus and phosphorites: Sedimentology and environments of formation. *Eclogae Geol. Helv.* **1994**, *87*, 747–788.

79. Parrish, J.T.; Droser, M.L.; Bottjer, D.J. A Triassic upwelling zone: The Shublik Formation, Arctic Alaska, USA. *J. Sediment. Res.* **2001**, *71*, 272–285. [CrossRef]

80. Harder, H. Synthesis of glauconite at surface temperatures. *Clays Clay Miner.* **1980**, *28*, 217–222. [CrossRef]

81. Gaudin, A.; Buatier, M.D.; Beaufort, D.; Petit, S.; Grauby, O.; Decareau, A. Characterization and origin of Fe^{3+}-montmorillonite in deep water calcareous sediments (Pacific Ocean, Costa Rica margin). *Clays Clay Miner.* **2005**, *53*, 452–465. [CrossRef]

82. Jiménez-Millán, J.; Castro, J.M. K-feldspar alteration to gel material and crystallization of glauconitic peloids with berthierine in Cretaceous marine sediments-sedimentary implications (Prebetic Zone, Betic Cordillera, SE Spain). *Geol. J.* **2008**, *43*, 19–31. [CrossRef]

83. Baldermann, A.; Dietzel, M.; Mavromatis, V.; Mittermayr, F.; Warr, L.N.; Wemmer, K. The role of Fe on the formation and diagenesis of interstratified glauconite-smectite and illite-smectite: A case study of Lower Cretaceous shallow-water carbonates. *Chem. Geol.* **2017**, *453*, 21–34. [CrossRef]

84. McCracken, S.R.; Compton, J.; Hicks, K. Sequence-stratigraphic significance of glaucony-rich lithofacies at Site 903. *G.S. Mt. Proc. ODP Sci. Results* **1996**, *150*, 171–187.

85. Myrow, P. Transgressive stratigraphy and depositional framework of Cambrian tidal dune deposits, Peerless Formation, Central Colorado, U.S.A. In *Tidalites: Processes and Products*; Alexander, C.R., Davis, R.A., Henry, V.J., Eds.; SEPM Special Publications: Broken Arrow, OK, USA, 1998; Volume 61, pp. 143–154.

86. Hesselbo, S.P.; Huggett, J.M. Glaucony in ocean margin sequence stratigraphy (Oligocene–Pliocene, Offshore New Jersey, USA.; ODP Leg 174A). *J. Sediment. Res.* **2001**, *71*, 598–606. [CrossRef]

87. Amorosi, A.; Guidi, R.; Mas, R.; Falanga, E. Glaucony from the Cretaceous of the Sierra de Guadarrama (Central Spain) and its application in a sequence stratigraphic context. *Int. J. Earth Sci.* **2011**, *1*, 415–427. [CrossRef]

88. Loutit, T.S.; Hardenbol, J.; Vail, P.R.; Baum, G.R. Condensed sections: The key to age determination and correlation of continental margin sequences. In *Sea-level Changes: An Integrated Approach*; Wilgus, C.K., Hastings, B.S., Kendall, C.G.S.C., Posamentier, H.W., Ross, C.A., Van Wagoner, J.C., Eds.; SEPM Special Publications: Broken Arrow, OK, USA, 1988; Volume 42, pp. 183–213.

89. Peters, S.E.; Gaines, R.R. Formation of the 'Great Unconformity' as a trigger for the Cambrian explosion. *Nature* **2012**, *484*, 363–366. [CrossRef]

90. Wigley, R.A.; Compton, J.S. Late Cenozoic evolution of the outer continental shelf at the head of the Cape Canyon, South Africa. *Mar. Geol.* **2006**, *226*, 1–23. [CrossRef]

91. Soares, A.M.; Martins, J.M. Radiocarbon dating of marine samples from Gulf of Cadiz: The reservoir effect. *Quat. Int.* **2010**, *221*, 9–12. [CrossRef]

92. Vargas, J.M.; García-Lafuente, J.; Delgado, J.; Criado, F. Seasonal and wind-induced variability of Sea Surface Temperature patterns in the Gulf of Cádiz. *J. Mar. Syst.* **2003**, *38*, 205–219. [CrossRef]

93. García-Lafuente, J.; Ruiz, J. The Gulf of Cádiz pelagic ecosystem: A review. *Prog. Oceanogr.* **2007**, *74*, 228–251. [CrossRef]

94. Fabião, C. O passado Proto-Histórico e Romano. A Romanização do actual território português. In *História de Portugal, Direcção de José Mattoso*; Mattoso, J., Ed.; Círculo de Leitores: Lisbon, Portugal, 1992; p. 567.